Infrared spectra and structures of $C_{60}Rh_n^+$ complexes

Estefania German [a],[*],[1], Gao-Lei Hou [b],[c],[1], Jan Vanbuel [b], Joost M. Bakker [d], Julio A. Alonso [a], Ewald Janssens [b], María J. López [a]

[a] Department of Theoretical, Atomic and Optical Physics, University of Valladolid, 47011, Valladolid, Spain
[b] Quantum Solid-State Physics, Department of Physics and Astronomy, KU Leuven, 3001, Leuven, Belgium
[c] MOE Key Laboratory for Non-Equilibrium Synthesis and Modulation of Condensed Matter, School of Physics, Xi'an Jiaotong University, Xi'an, 710049, Shaanxi, China
[d] FELIX Laboratory, Institute for Molecules and Materials, Radboud University, Nijmegen, the Netherlands

A B S T R A C T

Metal clusters supported on carbonaceous substrates are of interest in catalysis, hydrogen storage, and other fields. In this paper, the structures and the infrared spectra of $C_{60}Rh_n^+$ (n = 1–6) fullerene-metal complexes are studied by a combination of mass-selective infrared spectroscopy and theoretical calculations. It is found that clustering of Rh on the surface of the fullerene is preferred over surface wetting. For Rh_4^+ and Rh_6^+, the structures of the adsorbed clusters are different from those of the free clusters. There is electron transfer from the metal cluster to the fullerene in neutral $C_{60}Rh_n$, and in cationic $C_{60}Rh_n^+$ the electron deficit is shared by the metal cluster and the fullerene. Adsorption of Rh_n clusters leads to degeneracy lifting of the most intense C_{60} features in the infrared spectra that were measured in the 300–850 cm^{-1} range. Agreement is obtained, in general, between the experimental infrared spectra of D_2-tagged $C_{60}Rh_n^+$ and the calculated spectra for untagged $C_{60}Rh_n^+$, except in the 600–750 cm^{-1} region, where features mainly arise from the presence of D_2-messenger molecules adsorbed on the Rh_n clusters.

1. Introduction

Metal nanomaterials have been widely investigated in the past decades, both for fundamental research and for their potential application as catalysts in the chemical industry. Depending on the size of the metallic nanostructures, i.e., single atoms, few-atom clusters, or nanoparticles, they can exhibit different functionality in heterogeneous catalysis. The particle size, chemical composition, shape, and metal-support interaction are known to have significant influence on the properties of metal catalysts [1,2].

Supported metal catalysts are broadly employed in industry [3,4]. In many cases the support has the double function of stabilizing the adsorbed metal particles and of modifying their electronic structure and morphology through metal-support interactions [5,6]. The concept of strong metal-support interaction (SMSI) was introduced by Tauser et al. [7] to explain the observation that the adsorption of H_2 and CO on TiO_2–supported group 8 metals is dramatically suppressed after high-temperature reduction in H_2. The SMSI effect can significantly alter the catalytic properties [8] and can induce charge transfer and mass

transport between supports and metal particles [9–12]. Based on this concept, new catalysts with high activity have been developed [13–16]. Consequently, an improved understanding of the SMSI effect will impact innovations in catalyst development. In heterogeneous catalysis by supported metal nanostructures, intensive efforts have been dedicated to improve the performance by tuning the size of the metal particles. In fact, size, together with the nanoparticle structure, are critical ingredients in determining the reactivity and the efficiency of supported metal catalysts [17], through the specificity of active sites. Carbon materials are a class of very adaptable supports for heterogeneous catalysis, and they can easily be modified to generate a large surface area. A variety of carbon materials can be used as supports, such as activated carbons, nanotubes, graphene and graphene oxides [18,19].

Fullerene-metal complexes have attracted broad attention due to their potential applications in catalysis, superconductivity, hydrogen storage, and single-molecule electronics [20]. Previous studies have found that alkaline and alkaline earth metals tend to decorate or 'wet' the fullerene surface [21], whereas transition metals such as Co [22] prefer clustering on the surface. To better uncover the properties of these

---

materials, understanding about both the organization of the metal atoms on the support and their interaction is required.

In the current work we focus on rhodium, which is a widely used catalyst material. It is, for instance, an efficient catalyst for oxidation of ammonia in the production of nitric acid [23]. Catalysts based on supported rhodium are among the most active for direct nitrogen oxide (NO_x) decomposition. The selective removal of NO_x under lean-burn conditions is one of the most important aims in environmental catalysis research [24]. However, the catalysts suffer from rapid deactivation because of the saturation of metal active centers by adsorption of oxygen [25].

The aim of this work is to gain insight into the interaction and structural characteristics of rhodium adsorbed on carbon substrates, more specifically the C_{60} fullerene. Because both the geometric and electronic structures affect the catalytic activity, we have also studied the electronic charge transfer between cluster and support. Fullerene-metal complexes are ideal test benches to check these characteristics in a well-controlled environment. For example, Hou et al. have recently shown that a single vanadium atom supported on C_{60} can efficiently catalyze the water splitting process to produce H_2 upon infrared (IR) excitation, demonstrating the importance of carbonaceous supports in single atom catalysts [26,27]. IR spectroscopy is a powerful tool to determine structural characteristics of clusters and nanoparticles. The IR spectra of free Rh_n^+ clusters have been investigated using the far-IR multiple photon dissociation (IRMPD) spectroscopy of argon-tagged clusters [28]. Here, the same technique is used to measure the IR spectra of $C_{60}Rh_n^+$ complexes tagged with molecular deuterium. However, because D_2-tagging only provides an indirect way to measure the IR spectrum, it is important to perform a comparison between the experimental results and theoretical calculations on both D_2-tagged and untagged complexes, to check whether the IR spectra of D_2-tagged complexes reliably represent the IR spectra of the untagged ones.

2. Experimental methodology

The fullerene-rhodium complexes were synthesized in vacuum by a dual target dual laser source, which has been described in detail previously [22,29]. Briefly, a bulk rhodium target and a fullerene target, formed by cold-pressing C_{60} powder at a pressure of ~3 kbar, were vaporized by laser beams from two independent pulsed 532 nm Nd:YAG lasers, both operated at 10 Hz repetition rates, and carried by a pulse of helium gas (6 bar backing pressure). The vaporized C_{60} molecules and rhodium plasma collide with each other in the He gas, triggering the formation and cooling of $C_{60}Rh_n^+$ complexes. After formation, the gas mixture expanded into vacuum through a conical nozzle, forming a cluster beam, that is collimated by a 2 mm diameter skimmer and a 2 mm slit aperture, before entering a perpendicularly oriented reflectron time-of-flight (TOF) mass spectrometer. The experiments were performed with the cluster source at room temperature.

IR multiple photon dissociation (IRMPD) experiments were performed by overlapping the shaped cluster beam with the IR light of the Free Electron Laser for Intra-Cavity Experiments, FELICE [30]. The spectral range covered was 300–850 cm^{-1}. IR light was provided at a repetition rate of 5 Hz, or half the experimental repetition rate. This allowed to record successive mass spectra with and without IR laser interaction. IR excitation in resonance with a vibrational mode heats up the clusters by multiple photon absorption and intra-molecular vibrational redistribution (IVR). When the internal energy of the cluster is high enough, dissociation takes place on the time scale of the experiment, which can be sensitively probed by mass spectrometry.

Due to the high stability of $C_{60}Rh_n^+$ (calculated binding energies between C_{60} and Rh_n^+ are large; for example, 3.57 eV for $C_{60}Rh_1^+$, corresponding to approximately 48 photons at 600 cm^{-1}), the dissociation efficiency induced by the IR photon absorption is too low to obtain high quality IR spectra. Only the two IR absorption bands of highest IR oscillator strengths show up and even those have only a low signal-to-

noise (S/N) ratio (Fig. S1). Therefore, the messenger tagging technique was utilized, employing D_2 as tagging molecule. This technique has been well established in the past decades to obtain the vibrational spectra of molecular species via photodissociation [26,31,32]. D_2-tagged $C_{60}Rh_n^+$ complexes are synthesized by seeding about 0.5% of D_2 into the He carrier gas. D_2 readily desorbs from the complexes upon IR irradiation (the binding energy per D_2 molecule is about 0.8 eV, corresponding to approximately 10 photons at 600 cm^{-1}).

The free electron laser was scanned in wavenumber steps of 5 cm^{-1}. Out coupled light was used to reconstruct the intracavity laser power and to calibrate the wavelength using a grating spectrometer. A typical pulse energy is 1000 mJ at 400 cm^{-1}, while the spectral width of the laser amounts to ~0.6% of the central wavenumber with a typical uncertainty in wavenumber of ~0.2%.

In the current experiments, the lowest-energy fragmentation channel is the desorption of weakly-bound D_2 from $C_{60}Rh_n^+(D_2)_m$ (typical binding energy around 0.85 eV). Upon irradiation with IR light, the intensities of $C_{60}Rh_n^+(D_2)_m$ decrease, while those of $C_{60}Rh_n^+$ increase, pointing to D_2 desorption from the complexes. Since complexes tagged with multiple D_2 molecules exist in the molecular beam, care must be taken to analyze the intensity changes of both the bare and D_2-tagged $C_{60}Rh_n^+$. That is because not only can $C_{60}Rh_n^+(D_2)_m$ be photo fragmented by the IR laser, but it can simultaneously also be formed through IR-induced fragmentation of $C_{60}Rh_n^+(D_2)_{m+1}$. Such processes could appear in the spectrum of $C_{60}Rh_n^+(D_2)_m$ either as an unphysical, negative IRMPD yield, or lead to (partial) screening of the bands of $C_{60}Rh_n^+(D_2)_m$.

To account for this and to reduce noise originating from cluster synthesis fluctuations, we first calculate the branching ratio B_k of the mass spectrometric intensities I of the $C_{60}Rh_n^+(D_2)_m$ with at least k D_2 molecules:

$$B_k = \sum_{m=k}^{m_{max}} I\left[C_{60}Rh_n^+(D_2)_m\right] \bigg/ \sum_{m=0}^{m_{max}} I\left[C_{60}Rh_n^+(D_2)_m\right]. \tag{1}$$

Here m_{max} is the maximum number of attached D_2 molecules observed in the mass spectra for a specific n; k is chosen as the smallest number for which the cluster only shows D_2 loss under IR exposure and no ingrowth due to depletion of complexes with more D_2 molecules. This number varies with n: k = 1 for n = 1–3, k = 2 for n = 4, and k = 4 for n = 5, 6. Under the assumption of constant D_2 adsorption probabilities, the branching ratio eliminates shot-to-shot fluctuations in the particle synthesis, and changes in B_k reflect the loss of the kth D_2 molecule. The experiments allow to obtain IR spectra by comparing branching ratios without ($B_{k,0}$) and with ($B_k(\nu)$) irradiation at frequency ν.

The IRMPD yield $Y(\nu)$ is then obtained as the negative natural logarithmic depletion ratio corrected by the laser pulse energy $E(\nu)$ to account for variation of the laser power:

$$Y(\nu) = -\ln[B_k(\nu)/B_{k,0}] / E(\nu). \tag{2}$$

Note that IRMPD yields can generally deviate from linear IR absorption cross sections $\sigma(\nu)$ due to the multiple photon excitation process.

3. Computational methodology

Electronic and structural properties of $C_{60}Rh_n^+$ complexes with and without adsorbed deuterium were determined using *ab initio* Density Functional Theory (DFT), implemented in the Quantum-ESPRESSO suite of electronic structure codes, version 6.4.1 [33]. The Perdew-Burke-Ernzerhof generalized gradient approximation (GGA-PBE) was chosen for the exchange-correlation functional [34,35]. The electron-ion core interactions were modeled by the projected augmented wave method (PAW) [36,37]. The number of electrons treated explicitly is 17 for Rh ($4s^2 4p^6 4d^8 5s^1$), four for C ($2s^2 2p^2$), and one for H. The PAW pseudopotentials are available on the Quantum-ESPRESSO website [38]. A cutoff energy of 40 Ry was selected

for the plane waves used to expand the Kohn-Sham electronic orbitals, and 350 Ry for the charge density. The studied systems were modeled in a cubic supercell of $17 \times 17 \times 17$ Å^3, which has been checked to be large enough to assure no interaction among periodic images. The Γ point for the Brillouin zone integration was employed in the calculations. To account for dispersion corrections to the energy density functionals, which improve the description of the interaction between molecular hydrogen and $C_{60}Rh_n^+$, the Grimme-D3 method was used [39].

As the positive charge of the fullerene complexes gives rise to an electrostatic interaction between cells, the Makov-Payne correction was taken into account [40]. This correction is applied to calculate the total energy of an isolated charged system (a molecule or a cluster) modeled in a three-dimensional supercell with periodic boundary conditions. The method also provides an estimate of the vacuum level, so that eigenvalues can be properly aligned. The IR spectra in the harmonic approximation were obtained using the PHonon package, a part of Quantum-ESPRESSO [41].

The computational method has been evaluated by comparing our results for the adsorption of a Rh atom on C_{60} with previous studies of the adsorption of Rh on other carbon materials that were performed at the same level of theory. For instance, the interaction of Rh with carbon nanotubes has been investigated by Luna et al. [42], and with graphene by Ambrusi et al. [43] and Manade et al. [44], using the PAW method and the PBE exchange-correlation functional. Their calculated binding energies are 1.96 eV [43] and 2.01 eV [44] for Rh on pristine graphene, and 2.67 eV for Rh on (8,0) single-wall carbon nanotubes [42]. Our calculations obtained a binding energy of 2.50 eV for a Rh atom on C_{60} and a Rh–C bond distance of 2.045 Å, both close to those reported by Luna et al. for Rh on the (8,0) nanotube. The higher binding energies on nanotubes and fullerenes compared to graphene, are likely due to the different curvature of the carbon surface.

4. Experimental results

Fig. 1 presents mass spectra of $C_{60}Rh_n^+(D_2)_m$ without (black) and with (red) far-IR excitation at 520 cm^{-1}. It can be seen that $C_{60}Rh_n^+(D_2)_m$ complexes with n = 0–6 are formed. For all sizes n, D_2 adducts are formed, with the average number of D_2 adducts growing with n. Interestingly, the observed mass distributions are not smooth, with certain stoichiometries formed preferentially, such as $C_{60}Rh_1^+(D_2)_2$ or $C_{60}Rh_3^+(D_2)_4$. Overall, with increasing number of Rh atoms in $C_{60}Rh_n^+$, multiple D_2 molecule tagged complexes become dominant.

Fig. 2 presents the measured IRMPD spectra of $C_{60}Rh_n^+$ (n = 1–6) clusters. The two most intense features in all spectra appear around 520 and 570 cm^{-1}. These are likely due to characteristic vibrational modes for neutral C_{60}, as previous experiments have detected C_{60} modes at 527 and 570 cm^{-1} [45], or at 527 and 577 cm^{-1} [46]. Their frequencies are indicated with dashed vertical lines in Fig. 2. The spectra also show less

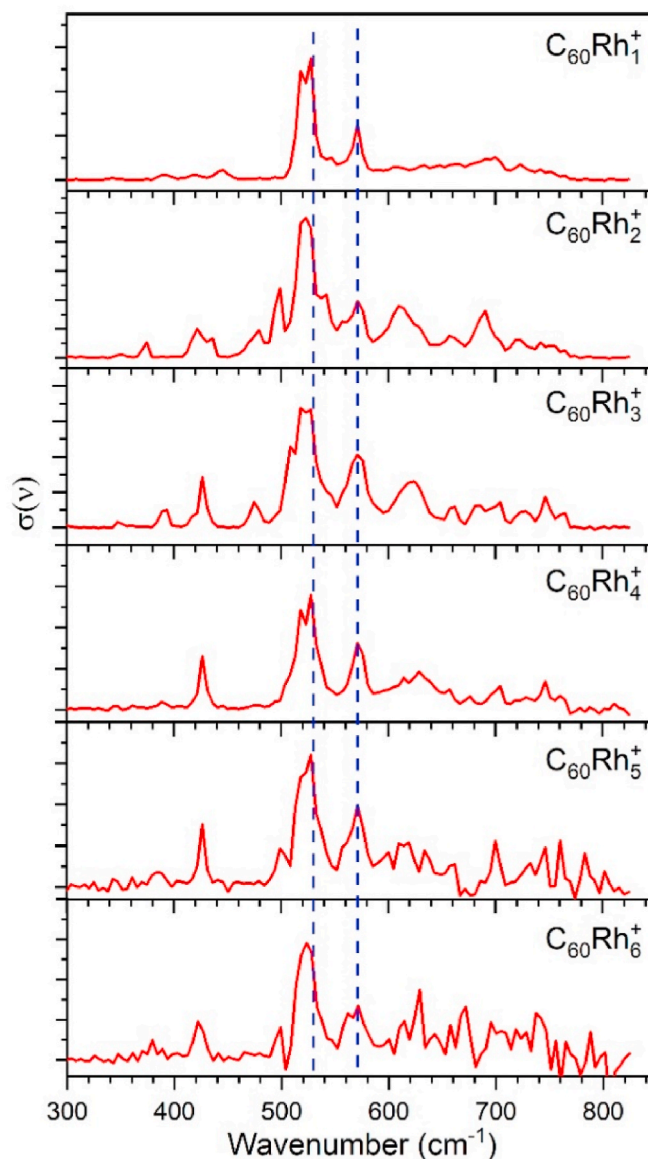**Fig. 2.** IRMPD spectra of D_2-tagged $C_{60}Rh_n^+$(n = 1–6). The vertical dashed lines indicate the gas-phase vibrational frequency positions of neutral C_{60} [45].

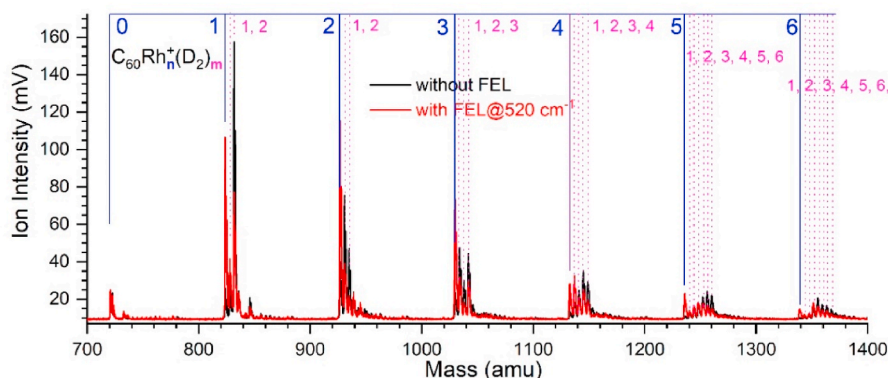**Fig. 1.** Mass spectra showing the mass distributions of $C_{60}Rh_n^+(D_2)_m$ without (black) and with (red) far-IR laser excitation at 520 cm^{-1}. The blue and magenta numbers correspond to n and m, respectively. (A colour version of this figure can be viewed online.)

intense modes at lower frequencies, around 420 cm^{-1}, and broader bands in the range 600–750 cm^{-1}. The observation of bands in these spectral regions suggests that they most likely are C$_{60}$ cage motions that become IR active (and are perturbed) by the adsorbed Rh$_n^+$ clusters and/or the tagged D$_2$ molecules. No Rh–Rh vibrational modes are expected in the 300–850 cm^{-1} spectral range since they have much lower frequencies [47]. A contribution of modes involving Rh–D$_2$ vibrations can be expected around 700–900 cm^{-1} based on previous studies of H$_2$ adsorption on Al$_n$Rh$^+$ (n = 1–12) clusters [48,49]. An analysis of the spectra and their comparison with theoretical calculations will be presented in the following sections.

5. Computational results and analysis

5.1. C$_{60}$Rh$_n^+$ complexes

Rh$_n$ adsorption on C$_{60}$ fullerene was studied computationally by sequentially adding Rh atoms. The lowest energy configuration (ground state, GS) and the first low-lying isomer, shown in Fig. 3 for each C$_{60}$Rh$_n^+$ complex, were found by optimizing a large number of possible initial structures allowing for variations of spin magnetic moments. We have considered different possibilities of a Rh atom (n = 1) interacting with the fullerene, namely, Rh adsorbed on top of a C atom, on a bridge site (interacting with a C=C double bond, or with a C–C single bond), and centered above a pentagon or a hexagon. For larger values of n, the Rh atoms are added in such a way that they interact with the surface of the fullerene: a) respecting the Rh–Rh bond distances; b) in the vicinity of the pre-adsorbed Rh atoms; c) in positions that are compatible with those obtained for smaller n.

Each structure in Fig. 3 is accompanied by the energy relative to the GS and the spin magnetic moment. In the GS configurations, the first

four Rh atoms are adsorbed on the fullerene in direct contact with the carbon atoms, forming a triangle for n = 3, and a square parallel to a fullerene hexagon for n = 4. For all the studied sizes, up to n = 6, the Rh$_n$ cluster is centered above a carbon hexagon (in the case of a single Rh atom, the atom is on a bridging site shared by two hexagons). Among the initial configurations explored, adsorption of the Rh$_n$ clusters on carbon pentagons was also studied. This was found to be less favorable than adsorption on hexagons, presumably due to the smaller area of the pentagon.

The Rh clusters on the fullerene become three-dimensional structures from n = 5 onward; Rh$_5$ and Rh$_6$ form pyramids with the respective square and pentagonal bases in contact with the fullerene. The energy differences of the first low-lying isomers with respect to the ground state (values are given in Fig. 3) vary substantially with n. For the first low-lying isomers, the number of Rh atoms in contact with the fullerene is at maximum three. For n = 4–6, the isomeric Rh$_n^+$ structures are a tetrahedron, a tetrahedron with one capped face and an octahedron, respectively.

In principle, the C$_{60}$Rh$_n$ complexes can form in two ways: by adding Rh atoms sequentially, and also by attaching the rhodium cluster to the fullerene. To gain insight into these two processes, two kinds of binding energies were calculated: The first one is the binding energy corresponding to the addition of a Rh atom (called here the nth atom) to the pre-formed C$_{60}$Rh$_{n-1}$ complex, calculated by subtracting the total energies of the final product from the reactants:

$$E_{binding}^{added\ atom}\left(n^{th}\ Rh\ atom\right) = E[(C_{60}Rh_{n-1})^+] + E[Rh] - E[(C_{60}Rh_n)^+]. \quad (3)$$

A positive sign indicates that the final product, C$_{60}$Rh$_n^+$, is more stable than the reactants. This can be also viewed as the energy required to remove a single Rh atom from C$_{60}$Rh$_n^+$. The second is the binding energy corresponding to the process of attaching a preformed Rh$_n^+$
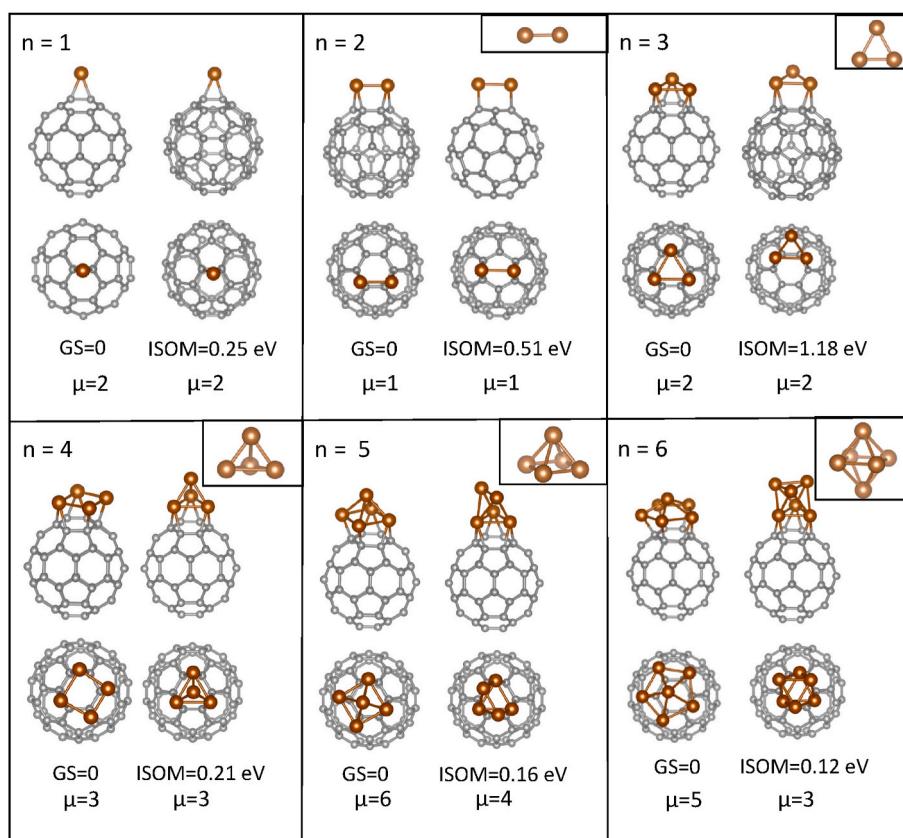

Fig. 3. Calculated ground state (GS, left), and first low-lying isomer (ISOM, right) structures of C$_{60}$Rh$_n^+$ (n = 1–6). Each panel contains a side view and a top view of the complex as well as an inset with the structure of the isolated Rh$_n^+$ cluster. Brown and grey spheres represent Rh and C atoms, respectively. Isomer energies above the ground state are indicated, as well as the spin magnetic moments μ (in units of μ$_B$). (A colour version of this figure can be viewed online.)

cluster on neutral C_{60}, calculated analogously:

$$E_{binding}^{cluster}\left(Rh_n^+\right) = E[C_{60}] + E\left[Rh_n^+\right] - E[(C_{60}Rh_n)^+] \tag{4}$$

In this equation, $E[Rh_n^+]$ is the total energy of the free Rh_n^+ cluster in its ground state. The calculated values of $E_{binding}^{added\ atom}(n^{th}\ Rh\ atom)$ and $E_{binding}^{cluster}(Rh_n^+)$ are given in Table 1. The atomic binding energies correspond to the energy gained upon addition of a single atom to $C_{60}Rh_{n-1}^+$. They reveal the role of the Rh–Rh interactions in the growth of the adsorbed metal cluster. Table 1 also includes the binding energies associated to the addition of a single Rh atom to form free Rh_n^+ clusters. These energies vary with n, as expected for small clusters, and have a maximum at n = 4, making Rh_4^+ a very stable (tetrahedral) cluster. The differences between the atomic binding energies in free Rh_n^+ and $C_{60}Rh_n^+$ show the 'substrate' effect of C_{60}. For n = 2 and 3, they are larger in the supported clusters due to the Rh–C_{60} interaction. The energy gain in the formation of $C_{60}Rh_4^+$ by this reaction is lower than that for free Rh_4^+ (3.98 eV vs 5.13 eV), because the structure of the supported Rh_4^+ is a square rather than a tetrahedron. A structural change also occurs for Rh_6^+, and the atomic binding energy in the supported clusters for n = 6 is lower than that of the free ones.

The energies for attaching intact (pre-formed) Rh_n^+ clusters to C_{60} reflect the interaction strength between the metal cluster and the fullerene and are dominated by the Rh–C interactions. The optimal cluster-fullerene matching occurs for Rh_3^+, with the three Rh atoms occupying bridge positions above C–C bonds, and the cluster-fullerene binding energy is the largest. For Rh_4^+–Rh_6^+, the cluster-fullerene matching is not optimal and the adsorption binding energy decreases in spite of the larger number of Rh atoms in direct contact with the fullerene (although the structural change also plays a role for Rh_4^+ and Rh_6^+).

The possibility of decoration of the fullerene with Rh atoms was also investigated, and the structures can be found in Supplementary Fig. S2. For this purpose, the configuration of two Rh atoms adsorbed on opposite sides of the fullerene, and three well-separated Rh atoms were considered, but those structures were found energetically much less favorable, 1.48 and 2.50 eV higher in energy, respectively, than the ground state structures given in Fig. 3. Also, structures with adsorbed Rh_2 and Rh_3 and with two adsorbed Rh_3 clusters in well separated locations of C_{60} were studied, but these alternative structures were also found much less stable (1.57 and 1.67 eV higher in energy) than the ground state structures of adsorbed Rh_5 and Rh_6, respectively. We conclude that Rh atoms prefer to aggregate in one metal cluster, instead of wetting the fullerene.

It has been noticed above that the interaction of the Rh clusters with the fullerene induces significant structural changes in Rh_4^+ and Rh_6^+ with respect to the configurations of the corresponding isolated clusters, but not for other cluster sizes (structures of isolated Rh_n^+ are shown as insets in Fig. 3). The isolated Rh_4^+ and Rh_6^+ have tetrahedral and octahedral structures, respectively. On the surface of the fullerene, Rh_n^+ clusters tend to maximize the number of Rh atoms in direct contact with C atoms. This is a significant difference with respect to cobalt cluster adsorption [22,50], in which case the calculations predicted a maximum of three Co atoms in direct contact with the fullerene. In the Rh case, up to five

atoms are in direct contact with the fullerene surface. This difference arises from a delicate balance between the strength of the metal-carbon and metal-metal interactions. In both cases (Rh and Co), the metal-metal interaction is stronger than the metal-fullerene interaction. This is confirmed by the results of the calculations discussed above, indicating that formation of Rh clusters on the fullerene surface is more favorable compared to wetting the surface, and the same occurs for Co on the fullerene [22,50]. However, the relative strength of the two interactions (metal-metal and metal-fullerene) is different for Rh–fullerene and Co–fullerene. We have estimated the relative strengths by first calculating the binding energies of a neutral Rh atom added to Rh_5^+ and to C_{60}^+, with $E_b(Rh–Rh_5^+) = 4.26$ eV, and $E_b(Rh–C_{60}^+) = 3.04$ eV, and then the binding energy difference $\Delta E_b(Rh) = E_b(Rh–Rh_5^+) - E_b(Rh–C_{60}^+) = 1.22$ eV. The corresponding binding energies for Co are $E_b(Co–Co_5^+) = 5.36$ eV, $E_b(Co–C_{60}^+) = 2.52$ eV, and the binding energy difference $\Delta E_b(Co) = E_b(Co–Co_5^+) - E_b(Co–C_{60}^+) = 2.84$ eV. Comparison of $\Delta E_b(Rh)$ and $\Delta E_b(Co)$ reveals that the strengths of the metal-metal and metal-fullerene interactions are more similar for Rh, than for Co, making it energetically more favorable for a larger number of Rh atoms to be in direct contact with the fullerene surface. Regarding wetting versus cluster formation, the numerical values of the binding energies between a Rh atom and C_{60}^+ (3.0 eV) or Rh_5^+ (4.26) might be used to illustrate the difference between Rh–C and Rh–Rh bond energies. These values explain the preference of cluster formation over wetting. However, as discussed above, the Rh clusters manage to adapt their geometrical structure to maximize the Rh–C bonding while maintaining the cluster compact, taking profit in this way of both Rh–Rh and Rh–C interactions.

The electronic charge transfer between metal clusters and the fullerene was studied by calculating the Bader atomic charges [51–53], shown in Table 2. The Bader charges reveal that the fullerene is negatively charged in neutral $C_{60}Rh_n$, in line with the fact that C_{60} is a good electron acceptor with an electron affinity of about 2.7 eV [54]. On the other hand, and more relevant for the present discussion, the electron deficit in $C_{60}Rh_n^+$ is shared by the metal cluster and the fullerene; but as the Rh_n size increases the positive charge becomes increasingly localized on the metal cluster, in such a way that in $C_{60}Rh_4^+$, $C_{60}Rh_5^+$ and $C_{60}Rh_6^+$ the C_{60} fragment is close to neutral. Charge densities plotted in Fig. S3 are consistent with the Bader charges.

5.2. Infrared spectra and comparison with experiment

Neutral C_{60} with its icosahedral symmetry has only four IR-active modes of T_{1u} symmetry experimentally found at 527.1, 570.3, 1169.1, and 1406.9 cm^{-1} [45]. These four modes are relatively well reproduced by our DFT calculations all exhibiting a slight overestimation that can be attributed to the harmonic approximation (Supplementary Fig. S4). The radical cation C_{60}^+ is Jahn-Teller active, distorting the icosahedral symmetry to D_{5d}. The reduction of symmetry makes several previously symmetry-forbidden IR transitions allowed, resulting in a less sparse IR spectra in comparison to that of the neutral (Fig. S4). Adsorption of Rh_n^+, regardless of where the resulting charge is localized, has a similar, but more pronounced symmetry breaking effect. For $C_{60}Rh_n^+$ (n = 1–3) some symmetry is retained, with C_{2v} (n = 1), C_s (n = 2) and C_{3v} (n = 3) respectively. For n = 4–6, the mismatch between the Rh_n bond distances

Table 1
Binding energies (in eV) of the last added Rh atom in Rh_n^+ and $C_{60}Rh_n^+$, and binding energy of the cationic Rh_n^+ cluster on the fullerene.

| n	$E_{binding}$ (eV)		
	Rh_{n-1}^+–Rh	$C_{60}Rh_{n-1}^+$–Rh	C_{60}–Rh_n^+
1		3.04	3.57
2	3.56	4.25	4.27
3	3.60	4.34	5.00
4	5.13	3.98	3.85
5	4.39	4.33	3.58
6	4.26	4.03	3.35

Table 2
Total electronic charges (in units of e) for Rh_n and C_{60} fragments in $C_{60}Rh_n$ and $C_{60}Rh_n^+$. A plus (minus) sign means that the fragment is positively (negatively) charged.

	Rh_n in $C_{60}Rh_n$	C_{60} in $C_{60}Rh_n$	Rh_n in $C_{60}Rh_n^+$	C_{60} in $C_{60}Rh_n^+$
n = 1	+0.23	- 0.23	+0.45	+0.55
n = 2	+0.33	- 0.33	+0.62	+0.38
n = 3	+0.45	- 0.45	+0.78	+0.22
n = 4	+0.50	- 0.50	+0.88	+0.12
n = 5	+0.57	- 0.57	+0.96	+0.04
n = 6	+0.56	- 0.56	+0.98	+0.02

and those in C_{60} leads to complete loss of symmetry, lifting all symmetry restrictions for IR activity. As a consequence, the calculated spectra for ground state structure and the first isomers of $C_{60}Rh_n^+$, $n = 1$–6 (shown in Fig. 4 together with that of C_{60}), show a wealth of IR active modes. Nevertheless, in the spectral region probed experimentally, the spectra still show dominant bands in the 500–600 cm^{-1} spectra range, originated from the triply degenerate T_{1u} modes of neutral C_{60}. Apart from these, new features appear in both the lower and higher frequency ranges. The differences between the IR spectra of the ground state structure and the first isomer of the $C_{60}Rh_n^+$ clusters are small, but more noticeable in $C_{60}Rh_4^+$, $C_{60}Rh_5^+$, and $C_{60}Rh_6^+$, as compared to $C_{60}Rh^+$, $C_{60}Rh_2^+$, and $C_{60}Rh_3^+$. The biggest differences are observed for $C_{60}Rh_6^+$, and this is confirmed by calculating the vibrational density of states of $C_{60}Rh_4^+$, $C_{60}Rh_5^+$, and $C_{60}Rh_6^+$, which are presented in Fig. S5 in the Supplementary Information.

The calculated IR spectra of untagged $C_{60}Rh_n^+$ (ground state and first
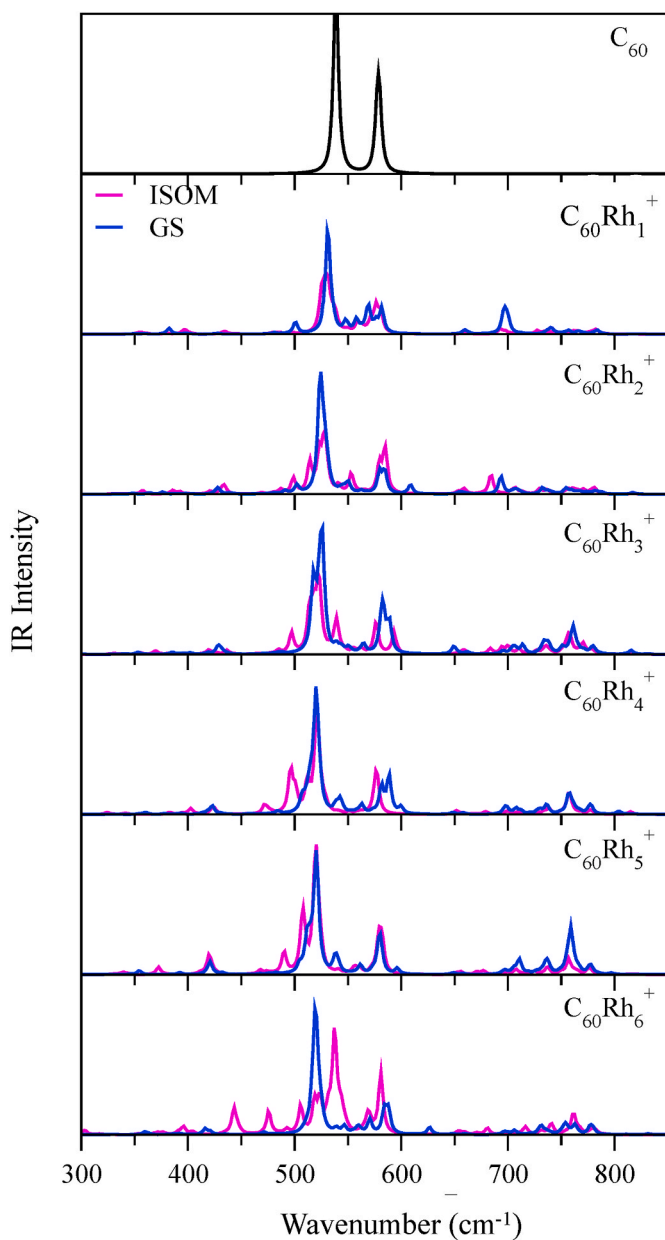
Fig. 4. Calculated IR spectra of C_{60} and $C_{60}Rh_n^+$. In each case, two spectra of $C_{60}Rh_n^+$ are compared. These correspond to the ground state (GS) and the first low-lying isomer structures (ISOM). (A colour version of this figure can be viewed online.)
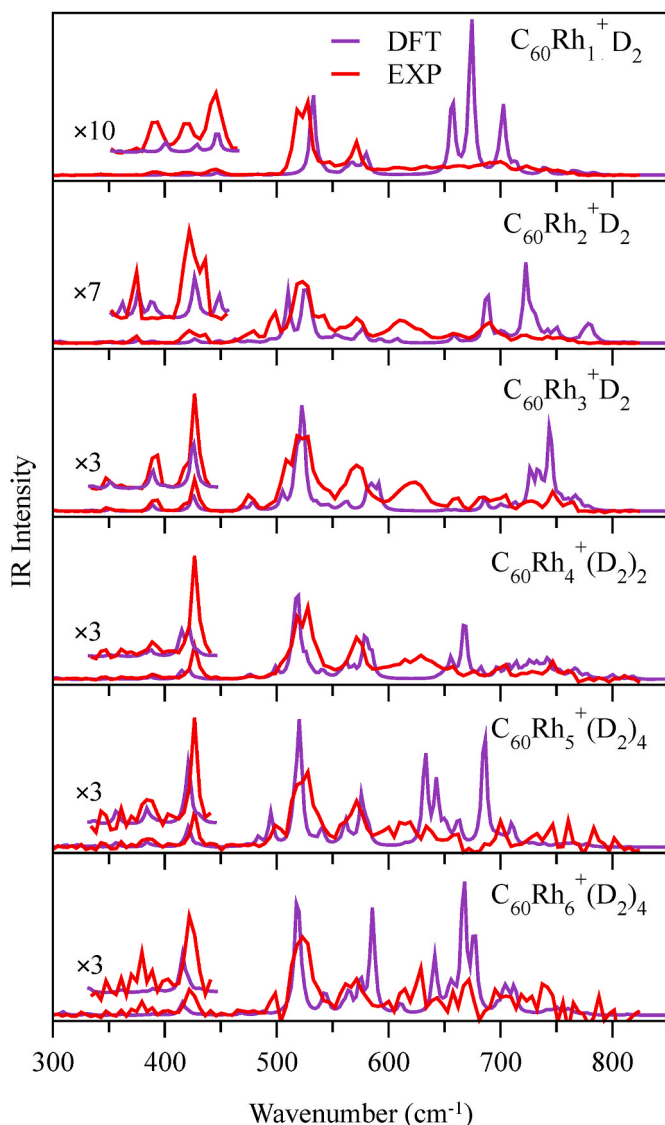
low-lying isomer structures) and the measured spectra of $C_{60}Rh_1^+D_2$, $C_{60}Rh_2^+D_2$, $C_{60}Rh_3^+D_2$, $C_{60}Rh_4^+(D_2)_2$, $C_{60}Rh_5^+(D_2)_4$, and $C_{60}Rh_6^+(D_2)_4$ are overlaid in Fig. S6 of the Supplementary Information. The main features in the experimental spectra of the deuterated clusters are reasonably well reproduced by the calculations for the GS structure of the untagged $C_{60}Rh_n^+$ clusters, except in the region between 600 and 800 cm^{-1}. Features of the experimental IR spectra in this frequency region appear to involve motions of the adsorbed deuterium molecules.

To inquire into the effect of the adsorbed deuterium, Fig. S7 shows the comparison between the calculated IR spectra of untagged $C_{60}Rh_n^+$ and deuterated $C_{60}Rh_1^+D_2$, $C_{60}Rh_2^+D_2$, $C_{60}Rh_3^+D_2$, $C_{60}Rh_4^+(D_2)_2$, $C_{60}Rh_5^+(D_2)_4$, and $C_{60}Rh_6^+(D_2)_4$. The lowest energy structures of the D_2-tagged complexes, shown in Fig. S8 of the Supplementary Information, reveal that adsorption of D_2 molecules does not strongly alter the structure of the underlying complexes. However, the deuteration leads to the appearance of very pronounced extra bands in the IR spectra, predominantly in the region between 600 and 750 cm^{-1}. This indicates in the current cases that D_2 may be regarded as a weakly bound messenger, because it mainly perturbs the vibrational spectra in the region between 600 and 750 cm^{-1}, and to a much lesser extent in other regions. The analysis of the atomic motions in the vibrational modes in this frequency region confirms the involvement of the D_2 molecules. Two specific examples are shown in Fig. S9 of the Supplementary Information. Outside the 600–750 cm^{-1} range, the only effect of D_2 adsorption is seen for $C_{60}Rh_2^+$, where the addition of one D_2 molecule leads to the amplification of a weak band around 510 cm^{-1}.

The activation barriers for the dissociation of molecular hydrogen on neutral and charged $C_{60}Co_n$ complexes vary with the size n of the metal cluster, but are in general small [22,50]. One may then ask if some of the D_2 molecules adsorbed on $C_{60}Rh_n^+$ are dissociated and this could be reflected in the IR spectra. The lowest energy structures of the $C_{60}Rh_n^+$ complexes with dissociated deuterium, are shown in Fig. S10 in the Supplementary Information. A comparison of the calculated IR spectra of complexes with dissociated and molecular deuterium, plotted in Fig. S11 of the Supplementary Information answers this question. The features introduced in the IR spectra by the dissociation of D_2 do not have a correspondence in the measured spectra. In particular, the measured features in the region 600-750 cm^{-1} are missing, indicating that these are due to the presence of molecular deuterium. Moreover, the calculated spectrum of $C_{60}Rh_1^+$ with dissociated D_2 exhibits an intense peak at 460 cm^{-1} which does not correspond to any experimental feature of the deuterated complex. This suggests that the complexes with dissociated deuterium are not present in the experiment.

Excluding the 600–800 cm^{-1} spectral region, it thus appears that the tagging with D_2 should allow for the faithful probing of the IR spectra of the $C_{60}Rh_n^+$ complexes. The studied frequency range, however, appears not diagnostic for a detailed comparison between different Rh_n^+ isomers since the Rh–Rh vibrations are expected at lower frequencies (below 350 cm^{-1}) [28].

Fig. 5 shows a comparison between the experimental IR spectra of the deuterated complexes $C_{60}Rh_1^+D_2$, $C_{60}Rh_2^+D_2$, $C_{60}Rh_3^+D_2$, $C_{60}Rh_4^+(D_2)_2$, $C_{60}Rh_5^+(D_2)_4$, and $C_{60}Rh_6^+(D_2)_4$ and the corresponding calculated spectra of those complexes with the adsorbed deuterium in molecular form. The main features and relative intensities of the bands in the region of frequencies corresponding to vibrations not involving D_2, are well reproduced by the calculations. Specifically, bands below 500 cm^{-1}, having been activated by the symmetry breaking due to the Rh_n adsorption, are predicted surprisingly accurately, as visible in the insets in Fig. 5. Less favorable is the comparison between experiment and calculations in the 600–750 cm^{-1} region. The calculated bands are much more intense and sharper than the observed band structure (for a better global presentation of the IR spectra, the calculated intensities for frequencies higher than 600 cm^{-1} have been divided by 2). This mismatch is striking, even considering that the calculated intensities are linear absorption cross-sections, while the experiment requires absorption of multiple photons. What is at the root of this mismatch is unclear.

Fig. 5. Comparison between the experimental IR spectra of $C_{60}Rh_1^+D_2$, $C_{60}Rh_2^+D_2$, $C_{60}Rh_3^+D_2$, $C_{60}Rh_4^+(D_2)_2$, $C_{60}Rh_5^+(D_2)_4$, and $C_{60}Rh_6^+(D_2)_4$, and the calculated spectra corresponding to molecular D_2 adsorption. The calculated intensities for frequencies higher than 600 cm^{-1} have been divided by 2. Zoom inserted for lower wavenumbers, $\times 10$, $\times 7$, $\times 3$ represent the magnification factor. (A colour version of this figure can be viewed online.)

We first note that in earlier IR spectroscopic experiments of metal clusters complexed with H_2, the bands assigned to H_2 wagging motion around the metal cluster were significantly shifted from the theoretical predictions [55,56]. One may thus doubt how accurate predictions for wagging motions could be in the first place. In the current calculations, no mode could be clearly identified as a pure D_2 wagging mode, as the normal modes calculated in this range all contain motions of the D_2 molecule combined with motions of the carbon atoms. One may further speculate that the exact orientation of the D_2 molecules (with both D atoms bound to the same Rh atom, see Fig. S8) could affect the precise frequency of wagging-like modes. We did not carry out extensive calculations on rotational isomers of the D_2 tag, but it could be expected that the D_2 orientation is quite flexible, leading to a potential dilution of the oscillator strength over a broader frequency range.

In contrast to the D_2 moieties, an analysis of the vibrational modes reveals that the Rh atoms do not contribute significantly to the vibrations in the frequency range presented in Fig. 5. Rh atoms are much heavier than the C and D atoms, and they mainly participate in

vibrational modes at lower wavenumbers. Calculated vibration modes involving Rh motion are found at frequencies from 26 to 300 cm^{-1}. Between 675 cm^{-1} and 850 cm^{-1} no participation of Rh in the vibrational modes is detected. However, a small contribution of the Rh atoms is found in the region from 350 to 674 cm^{-1}. That contribution only represents around a 5% of the total normalized phonon displacements: minimum and maximum values are 4.1% for $C_{60}Rh_1^+D_2$ and 6.1% for $C_{60}Rh_3^+D_2$, respectively.

6. Conclusions

The structures and the vibrational IR spectra of $C_{60}Rh_n^+$ complexes formed by Rh_n clusters ($n = 1$–6) adsorbed on the surface of the C_{60} fullerene have been investigated by a combination of experimental IR spectroscopy using the D_2-messenger technique and DFT calculations. The calculations predict that formation of Rh clusters on the surface of C_{60} is energetically preferred compared to wetting of the surface. In contrast to the free clusters, where Rh_4^+ is a tetrahedron, these are only three-dimensional for Rh_5 and Rh_6. The interaction with the C_{60} surface changes the geometric structure of Rh_4^+ and Rh_6^+ with respect to the configurations of the corresponding isolated clusters. The adsorption position of the Rh clusters is on top of carbon hexagon. The Rh_n clusters transfer electronic charge to the fullerene in the neutral $C_{60}Rh_n$ complexes, but in the cationic $C_{60}Rh_n^+$ complexes the electron deficit is shared by both the fullerene and the metal.

IR multiple photon dissociation spectra of $C_{60}Rh_n^+$ ($n = 1$–6) were measured with D_2-tagged complexes in the 300–850 cm^{-1} wavelength range. In this region, C_{60} has two IR-active modes at 527 and 570 cm^{-1}. The adsorption of Rh_n lifts the degeneracy of some vibration modes in the C_{60} IR spectrum. There is, in general, good agreement between the experimental $C_{60}Rh_n^+(D_2)_m$ IRMPD spectra and the calculated spectra for untagged $C_{60}Rh_n^+$, except in the region between 600 and 750 cm^{-1}, where experimentally observed features are much broader and at different frequencies than in the calculated IR spectra. Comparison with experiment and with calculations for tagged and untagged $C_{60}Rh_n^+$ clusters reveals that the features in the 600–750 cm^{-1} range, and to a lesser extent some features in other wavenumber ranges, are due to the presence of the D_2-messenger adsorbed on the Rh cluster.

CRediT authorship contribution statement

Estefania German: Investigation, Writing – original draft, Visualization, Formal analysis, Writing – review & editing. **Gao-Lei Hou:** Investigation, Writing – original draft, Visualization, Formal analysis, Writing – review & editing. **Jan Vanbuel:** Investigation, Methodology. **Joost M. Bakker:** Validation, Writing – review & editing. **Julio A. Alonso:** Conceptualization, Investigation, Writing – original draft, Writing – review & editing, Supervision. **Ewald Janssens:** Conceptualization, Writing – review & editing, Supervision, Funding acquisition. **María J. López:** Conceptualization, Writing – review & editing, Supervision, Funding acquisition.

Declaration of competing interest

The authors declare that they have no known competing financial interests or personal relationships that could have appeared to influence the work reported in this paper.

Appendix A. Supplementary data

Supplementary data to this article can be found online at https://doi.org/10.1016/j.carbon.2022.07.002.

References

[1] Y. Lou, J. Xu, Y. Zhang, C. Pan, Y. Dong, Y. Zhu, Metal-support interaction for heterogeneous catalysis: from nanoparticles to single atoms, Mater. Today Nano 12 (2020), 100093, https://doi.org/10.1016/j.mtnano.2020.100093.

[2] L. Liu, A. Corma, Metal catalysts for heterogeneous catalysis: from single atoms to nanoclusters and nanoparticles, Chem. Rev. 118 (2018) 4981–5079, https://doi.org/10.1021/acs.chemrev.7b00776.

[3] L. Peng, S.S.A. Shah, Z. Wei, Recent developments in metal phosphide and sulfide electrocatalysts for oxygen evolution reaction, Chin. J. Catal. 39 (2018) 1575–1593, https://doi.org/10.1016/S1872-2067(18)63130-4.

[4] J. Chi, H. Yu, Water electrolysis based on renewable energy for hydrogen production, Chin. J. Catal. 39 (2018) 390–394, https://doi.org/10.1016/S1872-2067(17)62949-8.

[5] Q. Zhang, X.X. Qin, F.P. Duan-Mu, H.M. Ji, Z.R. Shen, X.P. Han, W.B. Hu, Isolated platinum atoms stabilized by amorphous tungstenic acid: metal–support interaction for synergistic oxygen activation, Angew. Chem. Int. Ed. 57 (2018) 9351–9356, https://doi.org/10.1002/anie.201804319.

[6] A.S. Ivanova, E.M. Slavinskaya, R.V. Gulyaev, V.I. Zaikovskii, O.A. Stonkus, I. G. Danilova, L.M. Plyasova, I.A. Polukhina, A.I. Boronin, Metal–support interactions in Pt/Al2O3 and Pd/Al2O3 catalysts for CO oxidation, Appl. Catal., B 97 (2010) 57–71, https://doi.org/10.1016/j.apcatb.2010.03.024.

[7] S.J. Tauster, S.C. Fung, R.L. Garten, Strong metal-support interactions. Group 8 noble metals supported on titanium dioxide, J. Am. Chem. Soc. 100 (1978) 170–175, https://doi.org/10.1021/ja00469a029.

[8] G.L. Haller, D.E. Resasco, Metal–support interaction: group VIII metals and reducible oxides, Adv. Catal. 36 (1989) 173–235, https://doi.org/10.1016/S0360-0564(08)60018-8.

[9] L. Wang, J. Zhang, Y.H. Zhu, S.D. Xu, C.T. Wang, C.Q. Bian, X.J. Meng, F.S. Xiao, Strong metal–support interactions achieved by hydroxide-to-oxide support transformation for preparation of sinter-resistant gold nanoparticle catalysts, ACS Catal. 7 (2017) 7461–7465, https://doi.org/10.1021/acscatal.7b01947.

[10] T. Lunkenbein, J. Schumann, M. Behrens, R. Schlogl, M.G. Willinger, Formation of a ZnO overlayer in industrial Cu/ZnO/Al2O3 catalysts induced by strong metal–support interactions, Angew. Chem. Int. Ed. 54 (2015) 4544–4548, https://doi.org/10.1002/anie.201411581.

[11] H. Tang, F. Liu, J. Wei, B. Qiao, K. Zhao, Y. Su, C. Jin, L. Li, J. Liu, J. Wang, T. Zhang, Ultrastable hydroxyapatite/titanium-dioxide-supported gold nanocatalyst with strong metal–support interaction for carbon monoxide oxidation, Angew. Chem. Int. Ed. 55 (2016) 10606–10611, https://doi.org/10.1002/anie.201601823.

[12] B. Han, Y. Guo, Y. Huang, W. Xi, J. Xu, J. Luo, H. Qi, Y. Ren, X. Liu, B. Qiao, T. Zhang, Strong metal–support interactions between Pt single atoms and TiO2, Angew. Chem. Int. Ed. 59 (2020) 11824–11829, https://doi.org/10.1002/anie.202003208.

[13] Y.N. Sun, L. Giordano, J. Goniakowski, M. Lewandowski, Z.H. Qin, C. Noguera, S. Shaikhutdinov, G. Pacchioni, H.J. Freund, The Interplay between structure and CO oxidation catalysis on metal-supported ultrathin oxide films, Angew. Chem. Int. Ed. 49 (2010) 4418–4421, https://doi.org/10.1002/anie.201000437.

[14] T.W. van Deelen, C. Hernandez Mejía, K.P. de Jong, Control of metal-support interactions in heterogeneous catalysts to enhance activity and selectivity, Nat. Catal. 2 (2019) 955–970, https://doi.org/10.1038/s41929-019-0364-x.

[15] C. Liu, S.L. Nauert, M.A. Alsina, D. Wang, A. Grant, K. He, E. Weitz, M. Nolan, K. A. Gray, J.M. Notestein, Role of surface reconstruction on Cu/TiO2 nanotubes for CO2 conversion, Appl. Catal., B 255 (2019) 117754, https://doi.org/10.1016/j.apcatb.2019.117754.

[16] J. Li, Y. Lin, X. Pan, D. Miao, D. Ding, Y. Cui, J. Dong, X. Bao, Enhanced CO2 methanation activity of Ni/anatase catalyst by tuning strong metal–support interactions, ACS Catal. 9 (2019) 6342–6348, https://doi.org/10.1021/acscatal.9b00401.

[17] X.-F. Yang, A. Wang, B. Qiao, J. Li, J. Liu, T. Zhang, Single-atom catalysts: a new frontier in heterogeneous catalysis, Acc. Chem. Res. 46 (8) (2013) 1740–1748, https://doi.org/10.1021/ar300361m.

[18] C. Pham-Huu, M.-J. Ledoux, Carbon nanomaterials with controlled macroscopic shapes as new catalytic materials, Top. Catal. 40 (2006) 49–63, https://doi.org/10.1007/s11244-006-0104-8.

[19] P. Serp, M. Corrias, P. Kalck, Carbon nanotubes and nanofibers in catalysis, Appl. Catal., A 253 (2003) 337–358, https://doi.org/10.1016/S0926-860X(03)00549-0.

[20] M.A. Lebedeva, T.W. Chamberlain, A.N. Khlobystov, Harnessing the synergistic and complementary properties of fullerene and transition-metal compounds for nanomaterial applications, Chem. Rev. 115 (2015) 11301–11351, https://doi.org/10.1021/acs.chemrev.5b00005.

[21] D. Sankar De, J.A. Flores-Livas, S. Saha, L. Genovese, S. Goedecker, Stable structures of exohedrally decorated C60-fullerenes, Carbon 129 (2018) 847–853, https://doi.org/10.1016/j.carbon.2017.11.086.

[22] J. Vanbuel, E. Germán, K. Libeert, K. Veys, J. Moens, J.A. Alonso, M.J. López, E. Janssens, Reactivity of cobalt-fullerene complexes towards deuterium, ChemPhysChem 21 (10) (2020) 1012–1018, https://doi.org/10.1002/cphc.202000146.

[23] D.A. Bell, B.F. Towler, M. Fan, Coal Gasification and its Applications, Elsevier, 2011, https://doi.org/10.1016/B978-0-8155-2049-8.10011-7 (Chapter 11).

[24] A. Fritz, V. Pitchon, The current state of research on automotive lean NOx catalysis, Appl. Catal. B Environ. 13 (1997) 1–25, https://doi.org/10.1016/S0926-3373(96)00102-6.

[25] H. Beyer, K. Köhler, NOx removal by rhodium catalysts supported on carbon nanotubes: evidence for the stoichiometric reduction of NO2 and NO by the carbon support, Appl. Catal. B Environ. 96 (2010) 110–116, https://doi.org/10.1016/j.apcatb.2010.02.008.

[26] G.-L. Hou, T. Yang, M. Li, J. Vanbuel, O.V. Lushchikova, P. Ferrari, J.M. Bakker, E. Janssens, Water splitting by C60-supported vanadium single atoms, Angew. Chem. 60 (2021) 27095–27101, https://doi.org/10.1002/anie.202112398.

[27] M. Li, T. Yang, J.M. Bakker, E. Janssens, G.-L. Hou, Unveiling the role of C60-supported vanadium single atoms for catalytic overall water splitting, Cell Rep. Phys. Sci. 3 (2022) 1–13, 100910, https://10.1016/j.xcrp.2022.100910.

[28] D.J. Harding, P. Gruene, M. Haertelt, G. Meijer, A. Fielicke, S.M. Hamilton, W. S. Hopkins, S.R. Mackenzie, S.P. Neville, T.R. Walsh, Probing the structures of gas-phase rhodium cluster cations by far-infrared spectroscopy, J. Chem. Phys. 133 (2010), 214304, https://doi.org/10.1063/1.3509778.

[29] P. Ferrari, J. Vanbuel, Y. Li, T.-W. Liao, E. Janssens, P. Lievens, The double laser ablation source approach, in: Y. Huttel (Ed.), Gas-phase Synthesis of Nanoparticles, Wiley-VCH, 2017, pp. 59–78.

[30] J.M. Bakker, V.J.F. Lapoutre, B. Redlich, J. Oomens, B.G. Sartakov, A. Fielicke, G. von Helden, G. Meijer, A.F.G. van der Meer, Intensity–resolved IR multiple photon ionization and fragmentation of C60, J. Chem. Phys. 132 (2010), 074305, https://doi.org/10.1063/1.3313926.

[31] M. Okumura, L.I. Yeh, J.D. Myers, Y.T. Lee, Infrared spectra of the solvated hydronium ion: vibrational predissociation spectroscopy of mass-selected H3O+. (H2O)n.(H2)m, J. Phys. Chem. 94 (1990) 3416–3427, https://doi.org/10.1021/j100372a014.

[32] D.J. Goebbert, T. Wende, R. Bergmann, G. Meijer, K.R. Asmis, Messenger-tagging electrosprayed ions: vibrational spectroscopy of suberate dianions, J. Phys. Chem. A 113 (2009) 5874–5880, https://doi.org/10.1021/jp809390x.

[33] P. Giannozzi, S. Baroni, N. Bonini, M. Calandra, R. Car, C. Cavazzoni, D. Ceresoli, G.L. Chiarotti, M. Cococcioni, I. Dabo, et al., Quantum Espresso: a modular and open-source software project for quantum simulations of materials, J. Phys. Condens. Matter 21 (2009), 395502, https://doi.org/10.1088/0953-8984/21/39/395502.

[34] J.P. Perdew, K. Burke, M. Ernzerhof, Generalized gradient approximation made simple, Phys. Rev. Lett. 77 (1996) 3865–3868, https://doi.org/10.1103/PhysRevLett.77.3865.

[35] B. Hammer, L.B. Hansen, J.K. Nørskov, Improved adsorption energetics within density-functional theory using revised Perdew-Burke-Ernzerhof functionals, Phys. Rev. B 59 (1999) 7413–7421, https://doi.org/10.1103/PhysRevB.59.7413.

[36] G. Kresse, D. Joubert, From ultrasoft pseudopotentials to the projector augmented-wave method, Phys. Rev. B 59 (1999) 1758–1775, https://doi.org/10.1103/PhysRevB.59.1758.

[37] P.E. Blöchl, Projector augmented-wave method, Phys. Rev. B 50 (1994) 17953–17979, https://doi.org/10.1103/PhysRevB.50.17953.

[38] www.quantum-espresso.org/pseudopotentials.

[39] S. Grimme, J. Antony, S. Ehrlich, H. Krieg, A consistent and accurate ab initio parametrization of density functional dispersion correction (DFT-D) for the 94 elements H-Pu, J. Chem. Phys. 132 (2010), 154104, https://doi.org/10.1063/1.3382344.

[40] G. Makov, M.C. Payne, Periodic boundary conditions in ab initio calculations, Phys. Rev. B 51 (1995) 4014–4022, https://doi.org/10.1103/PhysRevB.51.4014.

[41] P. Giannozzi, O. Andreussi, T. Brumme, O. Bunau, M. Buongiorno Nardelli, M. Calandra, R. Car, C. Cavazzoni, D. Ceresoli, et al., Advanced capabilities for materials modelling with Quantum ESPRESSO, J. Phys. Condens. Matter 29 (2017), 465901, https://doi.org/10.1088/1361-648X/aa8f79.

[42] C.R. Luna, V. Verdinelli, E. German, H. Seitz, M.A. Volpe, C. Pistonesi, P.V. Jasen, Hydrogen adsorption and associated electronic and magnetic properties of Rh-decorated (8,0) carbon nanotubes using Density Functional Theory, J. Phys. Chem. C 119 (2015) 13238–13247, https://doi.org/10.1021/acs.jpcc.5b01407.

[43] R.E. Ambrusi, C.R. Luna, A. Juan, M.E. Pronsato, DFT study of Rh-decorated pristine, B-doped and vacancy defected graphene for hydrogen adsorption, RSC Adv. 6 (2016) 83926–83941, https://doi.org/10.1039/C6RA16604K.

[44] M. Manade, F. Viñes, F. Illas, Transition metal adatoms on graphene: a systematic density functional study, Carbon 95 (2015) 525–534, https://doi.org/10.1016/j.carbon.2015.08.072.

[45] C.I. Frum, R. Engleman, H.G. Hedderich, P.F. Bernath, L.D. Lamb, D.R. Huffman, The infrared emission spectrum of gas-phase C_{60} (buckmisterfullerene), Chem. Phys. Lett. 176 (1991) 504–508, https://doi.org/10.1016/0009-2614(91)90245-5.

[46] D.S. Bethune, G. Meijer, W.C. Tang, H.J. Rosen, W.G. Golden, H. Seki, C.A. Brown, M.S. de Vries, Vibrational Raman and infrared spectra of chromatographically separated C_{60} and C_{70} fullerene clusters, Chem. Phys. Lett. 179 (1991) 181–186, https://doi.org/10.1016/0009-2614(91)90312-W.

[47] D.J. Harding, P. Gruene, M. Haertelt, G. Meijer, A. Fielicke, S.M. Hamilton, W. S. Hopkins, S.R. Mackenzie, S.P. Neville, T.R. Walsh, Probing the structures of gas-phase rhodium cluster cations by far-infrared spectroscopy, J. Chem. Phys. 133 (2010), 214304, https://doi.org/10.1063/1.3509778.

[48] M. Jia, J. Vanbuel, P. Ferrari, E.M. Fernández, S. Gewinner, W. Schöllkopf, M. T. Nguyen, A. Fielicke, E. Janssens, Size dependent H_2 adsorption on Al_nRh^+ (n = 1–12) clusters, J. Phys. Chem. C 122 (2018) 18247–18255, https://doi.org/10.1021/acs.jpcc.8b04332.

[49] M. Jia, J. Vanbuel, P. Ferrari, W. Schöllkopf, A. Fielicke, M.T. Nguyen, E. Janssens, Hydrogen adsorption and dissociation on $Al_nRh_2^+$ (n = 1 to 9) clusters: steric and coordination effects, J. Phys. Chem. C 124 (2020) 7624–7633, https://doi.org/10.1021/acs.jpcc.8b04332.

[50] E. German, J.A. Alonso, E. Janssens, M.J. López, $C_{60}Co_n$ complexes as hydrogen adsorbing materials, Int. J. Hydrogen Energy 46 (2021) 20594–20606, https://doi.org/10.1016/j.ijhydene.2021.03.179.

[51] R.F.W. Bader, Atoms in molecules, Acc. Chem. Res. 18 (1985) 9–15, https://doi.org/10.1021/ar00109a003.

[52] R.F.W. Bader, Atoms in Molecules-A Quantum Theory, Oxford University Press, Oxford, 1990.

[53] W. Tang, E. Sanville, G. Henkelman, A grid-based Bader analysis algorithm without lattice bias, J. Phys. Condens. Matter 21 (2009), 084204, https://doi.org/10.1088/0953-8984/21/8/084204.

[54] X.B. Wang, C.F. Ding, L.S. Wang, High resolution photoelectron spectroscopy of C60-, J. Chem. Phys. 110 (1999) 8217–8220, https://doi.org/10.1063/1.478732.

[55] I. Swart, P. Gruene, A. Fielicke, G. Meijer, B.M. Weckhuysen, F.M.F. de Groot, Molecular adsorption of H_2 on small cationic nickel clusters, Phys. Chem. Chem. Phys. 10 (37) (2008) 5743–5745, https://doi.org/10.1039/B807313A.

[56] O.V. Lushchikova, H. Tahmasbi, S. Reijmer, R. Platte, J. Meyer, J.M. Bakker, IR spectroscopic characterization of H_2 adsorption on cationic Cu_n^+ (n = 4–7) clusters, J. Phys. Chem. A 125 (14) (2021) 2836–2848, https://doi.org/10.1021/acs.jpca.0c11527.